Solar Physics (2005) 225: 75–90

MULTI-WAVELENGTH OBSERVATION RESULTS OF THE C5.6 LIMB FLARE OF 1 AUGUST 2003

HUI LI, JIANQI YOU, QIUSHENG DU and XINGFENG YU
Purple Mountain Observatory, Chinese Academy of Sciences, Nanjing 210008, China

(Received 22 April 2004; accepted 11 August 2004)

Abstract. We obtained a complete set of Hα, Ca II 8542 Å and He I 10830 Å spectra and slit-jaw Hα images of the C5.6 limb flare of 1 August 2003 using the Multi-channel Infrared Solar Spectrograph (MISS) at Purple Mountain Observatory. This flare was also observed by the Reuven Ramaty High-Energy Solar Spectroscopic Imager (RHESSI) and partially by the Extreme-ultraviolet Imaging Telescope (EIT) on SOHO. This flare underwent a rapid rising and expanding episode in the impulsive phase. All the Hα, Ca II 8542 Å and He I 10830 Å profiles of the flare are rather wide and the widest profiles were observed in the middle bright part of the flare instead of at the flare loop top near the flare maximum. The flare manifested obvious rotation in the flare loop and the decrease of the rotation angular speed with time at the loop-top may imply a de-twisting process of the magnetic field. The significant increases of the Doppler widths of these lines in the impulsive phase reflect quick heating of the chromosphere, and rapid rising and expanding of the flare loop. The RHESSI observations give a thermal energy spectrum for this flare, and two thermal sources and no non-thermal source are found in the reconstructed RHESSI images. This presumably indicates that the energy transfer in this flare is mainly by heat conduction. The stronger thermal source is located near the solar limb with its position unchanged in the flare process and spatially coincident with the intense EUV and Hα emissions. The weaker one moved during the flare process and is located in the Hα dark cavities. This flare may support the theory of the magnetic reconnections in the lower solar atmosphere.

1. Introduction

Solar flare spectroscopy is a key tool for solar flare physics. In addition to providing detailed information of the flaring plasma on solar element abundances, turbulent velocities, electron temperatures and densities (Suemoto and Hiei, 1959; Švestka, 1976; Li *et al*., 2002a; Gu, Dun, and Zhong, 2003), high-resolution flare spectra can also provide unambiguous information on the dynamics of individual solar structures (Mariska, 1994; Bentley, Doschek, and Mariska, 1996; Brosius, 2001; Morimoto and Kurokawa, 2003; Qiu and Gary, 2003). Meanwhile, flare spectral profiles can be used to distinguish whether the flaring plasma was bombarded by high-energy electron beams (Canfield and Gayley, 1987; Fang, Hénoux, and Gan, 1993). Ground- and space-based multi-wavelength observations of solar flares from microwave to hard X-ray (HXR) allow us to determine physical parameters and dynamical process of flaring plasma in a wide temperature range of 10^4–10^7 K and in different layers of the solar atmosphere from the chromosphere to the transition region (Ding, Liu, and Chen, 2002; Liu and Ding, 2002; Gallagher *et al*., 2002; Falchi *et al*., 2003; Heinzel, 2003; Kundu *et al*., 2004).

Early spectroscopic observations and theoretical studies of solar flares were done mainly in Hα, Hβ and Ca II K lines (Hénoux, Fang, and Gan, 1993; Fang, Hénoux, and Ding, 2000). Recently, they were extended to some infrared lines, such as Ca II 8542 Å and He I 10830 Å lines (Ding, Liu, and Chen, 2002; You *et al*., 1998, 2001). Spectral lines are thought to be wide in solar limb flares (Švestka, 1976). The Hα and He I 10830 Å line profiles are shown to be unusually broadened in solar limb flares (Ding *et al*., 1999; You *et al*., 1998), whereas the Ca II 8542 Å line was observed to be narrow in a limb flare (Ding *et al*., 1999). The unusually broadened profiles in limb flares were simulated by the broadenings of micro-turbulence and/or inhomogeneous mass motion (Ding *et al*., 1999), the bombardment of non-thermal electrons (Fang, Hénoux, and Ding, 2000) and the expanding flaring atmosphere model (Li and You, 2001). We need more simultaneous spectroscopic observations of solar limb flares in multiple lines to ascertain whether all spectral lines in limb flares are considerably wide as well as to discriminate among diverse broadening mechanisms, such as Stark effects, thermal motions, non-thermal electron bombardment and expanding flaring plasma motions.

Simultaneous observations of solar flares in Hα and Ca II 8542 Å (Mein *et al*., 1997; Ding *et al*., 1999), or in Ca II 8542 Å and He I 10830 Å (You *et al*., 2001) have been reported. However, there is no simultaneous observation report of solar flares (both disk and limb flares) in all the three lines so far. We observed the C5.6 limb flare of 1 August 2003 in Hα, Ca II 8542 Å and He I 10830 Å simultaneously. This flare was also observed by some space instruments (see next section for details). It is suitable for addressing aforementioned aspects of solar limb flare study. In this paper, we present, for the first time, the results from simultaneous observations of this flare in all the earlier three lines.

In the following sections, we will briefly describe the observations and data reductions (Section 2), present the observational results (Section 3), and give our conclusions and discussions (Section 4).

2. Observations and Data Reductions

The C5.6 limb flare studied in this paper started at 01:19 UT, peaked at 01:26 UT and ended at 01:32 UT on 1 August 2003 according to GOES X-ray observations. There is no Hα record of this flare in the Solar Geophysical Data (SGD). Our Hα observation was made by the slit-jaw system of the Multi-channel Infrared Solar Spectrograph (MISS) (Li, Fan, and You, 1999; Li *et al*., 2002b) at Purple Mountain Observatory (PMO), which uses a Daystar filter with 0.5 Å passband. The slit-jaw Hα images taken in the period of 01:19–01:34 UT indicate that the Hα flare started at 01:20 UT and peaked at 01:27 UT. We obtained the Hα, Ca II 8542 Å and He I 10830 Å spectra using the MISS at PMO with integrating times of 0.06, 0.06 and 0.4 s, respectively. The spatial resolution is 1.34″ along the slit after four-row binning in the observation, and the spectral dispersion is 0.05453, 0.05113 and

0.04776 Å per pixel for Hα, Ca II 8542 Å and He I 10830 Å, respectively. The observed spectral data were corrected for the dark-current, flat-field and instrument profile, and absolutely calibrated by using the disk-center continuum intensity near these wavelengths.

We took disk-center spectra before and after the observation of the flare, which were used to calibrate the flare spectral data. The intensity calibration uncertainty is related to the signal to noise (S/N) ratio, and subsequently to the exposure times of both the disk-center and flare spectrograms. The estimated relative errors of the intensity calibrations for the three lines of this limb flare are 2–4%.

We use a mercury lamp to illuminate the slit of the spectrograph to obtain the profiles of HgI 5769 Å and HgI 10142 Å. The instrumental profile for Hα was derived from the HgI 5769 Å profile and those for Ca II 8542 Å and He I 10830 Å from the HgI 10142 Å profile. We applied the derived instrumental profiles to the disk-center spectra of the quiet Sun and compared the de-convolved spectral profiles with those observed by Kitt Peak Observatory. They are consistent within a relative error of $\leq$3%.

There is no high-resolution EUV observation from the Transition Region and Coronal Explorer (TRACE) because it was pointed to another active region. The EUV images at 195 Å used in this paper were observed by the Extreme-ultraviolet Imaging Telescope (EIT) (Delaboudinière *et al.*, 1995) on board the Solar and Heliospheric Observatory (SOHO) (Domingo, Fleck, and Poland, 1995). The Hard X-ray data are from the Reuven Ramaty High-Energy Solar Spectroscopic Imager (RHESSI) (Lin *et al.*, 2002). The full-disk intensity gram, which was used to coalign our Hα, EIT and RHESSI images, was observed by the Michelson Doppler Imager (MDI) (Scherrer *et al.*, 1995) on SOHO.

3. Observational Results

This C5.6 flare occurred in the active region NOAA 10424, which was located at the south-east limb of the Sun and not numbered in SGD on 1 August 2003. AR 10424 was located at S18E77 on 00:00 UT of 2 August according to SGD, and produced three X-ray flares of class M in the following days. In this section, we describe our observational results.

3.1. Hα AND SPECTROSCOPIC EVOLUTION

In our Hα observation, the Hα flare was first detected at 01:20 UT and peaked at 01:27 UT. Figure 1 shows a time sequence of the Hα images and Figure 2 the corresponding Hα, Ca II 8542 Å and He I 10830 Å spectrograms. We have only Ca II 8542 Å and He I 10830 Å spectrograms for the Hα image at 01:20:26 UT due to delayed response of the computer for Hα spectroscopic observation. We plot in Figure 3 the widest Hα, Ca II 8542 Å and He I 10830 Å profiles of each

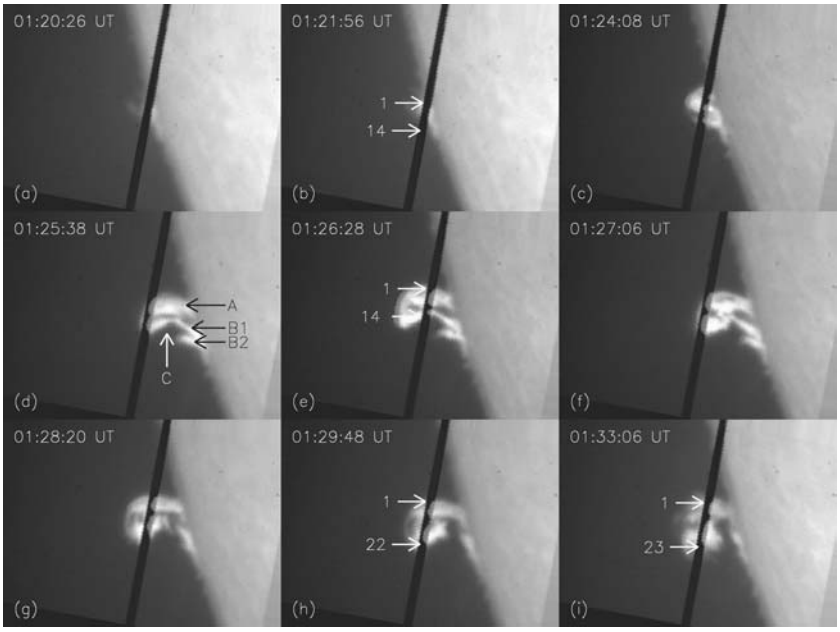

Figure 1. Slit-jaw Hα images observed by the MISS at PMO. The image size is $170'' \times 128''$. North is at the top and east to the left. The letters in (d) denote the footpoints of the flare loop (A, B1 and B2) and the dark cavity (C) discussed in the text. The observation time is given at the upper-left corner of each image. The numbered arrows in (b), (e), (h) and (i) indicate the start and end positions on the slit corresponding to the plots of the first to the fourth rows in Figure 5 respectively.

spectrogram in Figure 2, which were absolutely calibrated by using the disk-center spectral data and continuum intensity. It is worth mentioning that the profiles in Figure 3 correspond to the widest ones observed along the slit at the given time and the changes observed from frame to frame are due to both temporal and spatial variations.

At the beginning of the flaring process, the flare was just a small bright mound at the south-east limb of the Sun (Figure 1(a)), Hα and He I 10830 Å spectra show weak emission and blue-shifted profiles (Figures 2(a) and 2(b), and 3(a) and 3(b)). The area of the Hα flare increased gradually (Figure 1(b)) and the Hα flare loop was formed near 01:24:08 UT (Figure 1(c)). The spectral emissions, line-center intensities and line widths of all three lines increased (Figures 2(c)–2(h) and 3(c)–3(h)). From 01:21:56 to 01:24:08 UT, the line-center intensity of Hα was increased by about 60% (Figures 2(c) and 2(f)), whereas the line intensities of Ca II 8542 Å and He I 10830 Å did not show much increment. On the other hand, all the three lines show large increments in line widths.

The Hα flare loop then rose and expanded quickly and reached its maximum height and area at about 01:27 UT (Figures 1(d)–1(f)). The estimated average rising speed of the loop in the sky plane from the Hα images in the period of

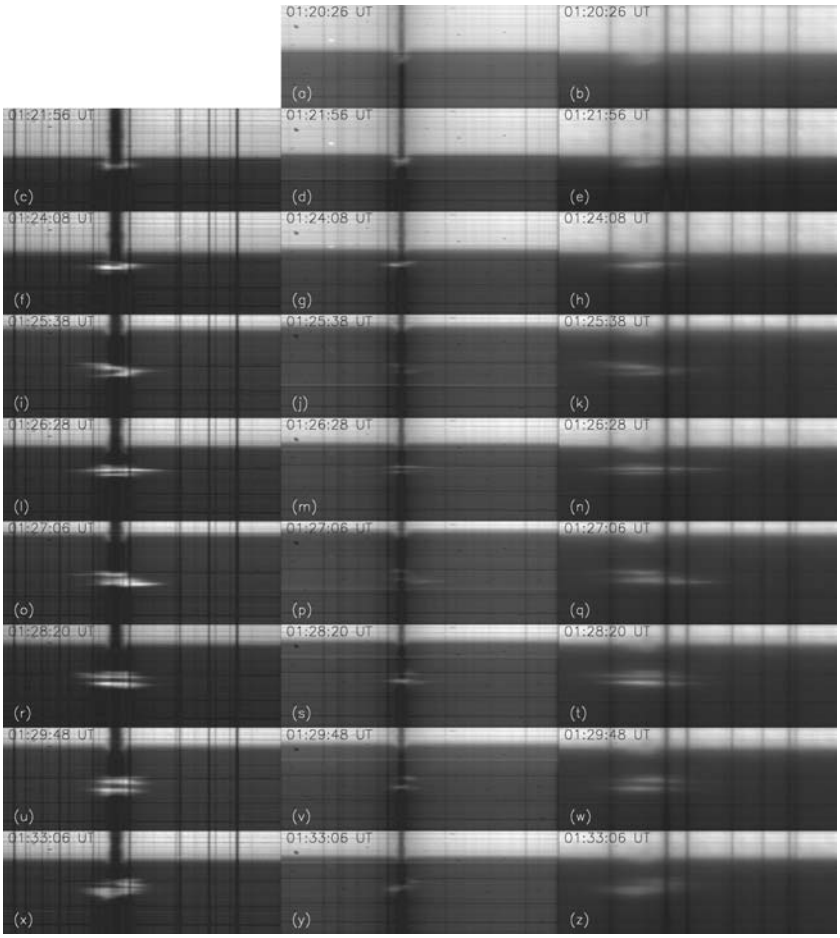

Figure 2. Hα (*left*), Ca II 8542 Å (*middle*) and He I 10830 Å (*right*) spectrograms observed by the MISS at PMO, which correspond to the Hα images in Figure 1. Observation times are indicated in each spectrogram.

01:24:08–01:25:38 UT is 152 km s^{-1}, which presumably indicates the rapid rising of the flux tube into the corona. The Hα images in this period and later, displayed dark cavities in the central part that is labeled C in Figure 1(d). The south footpoint of the loop in Hα images consists of two parts: the northern one (B1) is a part of the closed Hα loop and the southern one (B2) appears to be a small jet and is not connected to the loop (Figure 1(d)). However, we will see in the next section that it is actually a part the EUV loop of the flare (Figure 4(a)). During this period, the line-center intensities of Hα, Ca II 8542 Å and He I 10830 Å did not change much, whereas their Doppler widths kept increasing (Figures 2(i)–2(q) and 3(i)–3(q)). The spectrograms at the loop top showed tilted structures (Figures 2(i)–2(k) and 2(o)–2(q)) that indicate rotating motion of the plasma in the loop. The derived angular

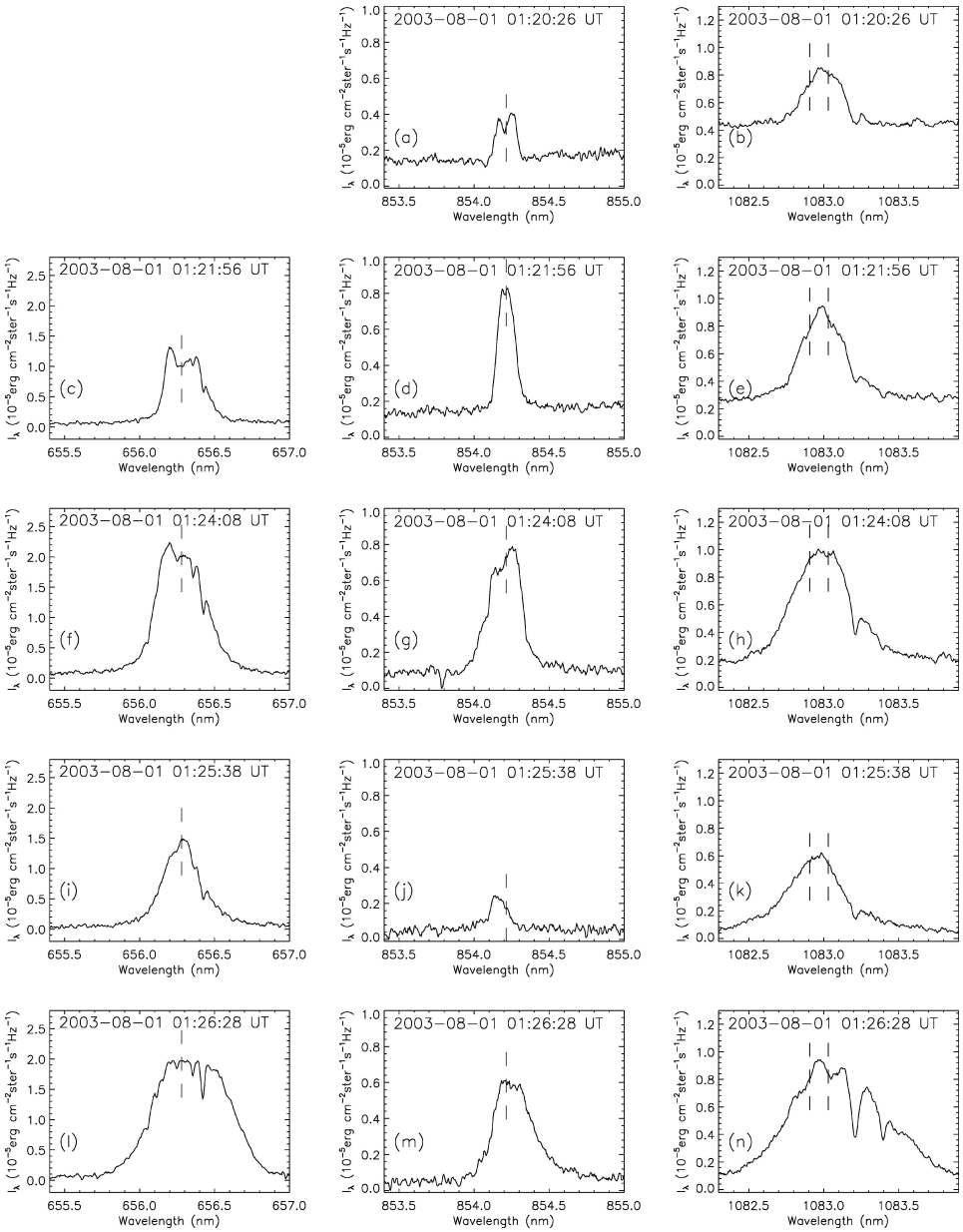

Figure 3. Widest Hα (*left*), Ca II 8542 Å (*middle*) and He I 10830 Å (*right*) profiles corresponding to the spectrograms in Figure 2. The line intensities are absolutely calibrated and given in units of erg cm^{-2} ster^{-1} s^{-1} Hz^{-1}. The *dashed vertical bars* in the plots indicate the rest wavelengths of Hα, Ca II 8542 Å and the I_{12} and I_3 components of the He I 10830 Å line. The observation times are shown in each plot.

(*Continued on next page*)

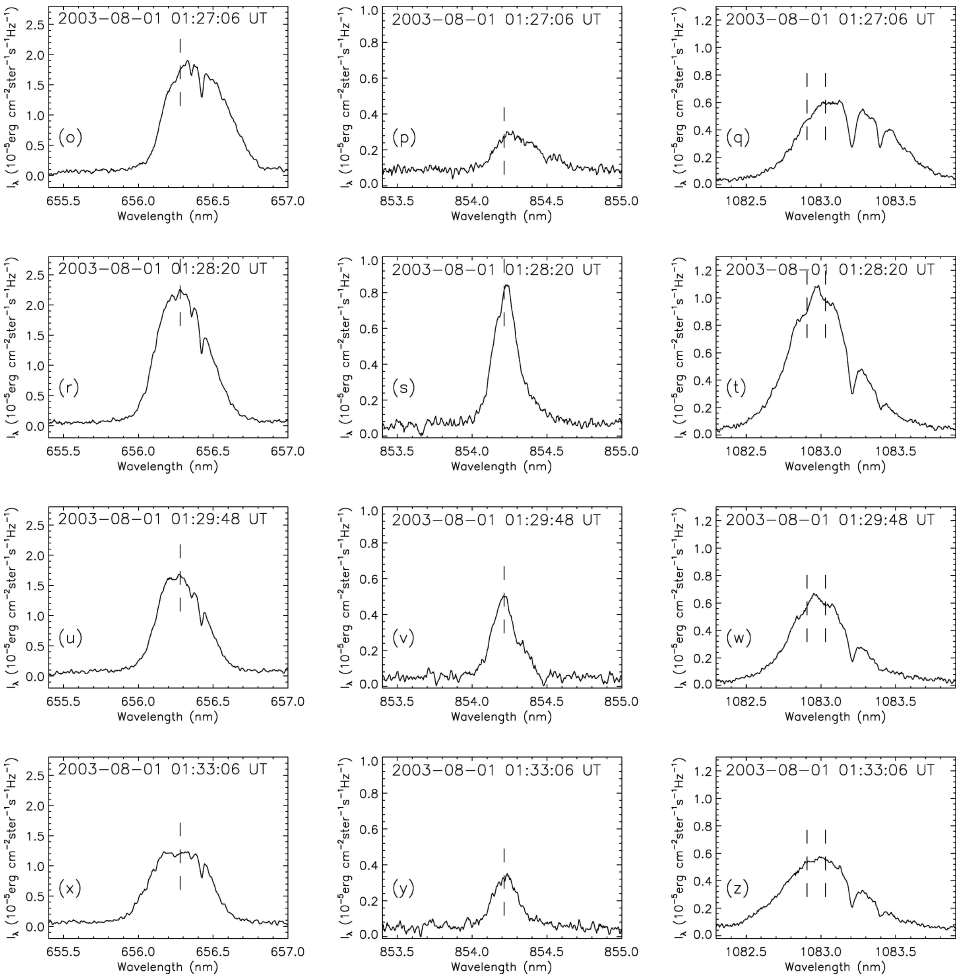

Figure 3. (*Continued*)

speeds at 01:25:38 UT and 01:27:06 UT are 9.6 and 5.8 $\times 10^{-3}$ rad s^{-1}, respectively. The decrease of rotation speed with time probably implies a de-twisting process of the magnetic field in the flare loop. The widest profiles of these three lines were observed near 01:26:28 UT in the middle part of the flare (Figures 2(l)–2(n) and 3(l)–3(n)) (cf. Section 3.3). The maximum full width at half maximum (FWHM) for Hα, Ca II 8542 Å and He I 10830 Å are 4.2, 3.18 and 5.78 Å, respectively. The corresponding Doppler widths ($\Delta\lambda_D = 0.6006 \times$ FWHM) for the three lines are 2.57, 1.91 and 3.47 Å, which require non-thermal velocities of 116, 67 and 96 km s^{-1}, respectively, assuming Doppler broadening of a uniform flare model with a temperature of 10^4 K. These values are much larger than the commonly accepted ones, implying that there exists strong turbulence in this flare.

After 01:27 UT, the flare began to decay and the flare loop gradually weakened and dispersed (Figures 1(g)–1(i)). The southern leg (B1 + B2) of the flare loop decayed more quickly than the northern one (A). As a consequence, the flare loop appeared to be a dispersed plasma cloud that anchored to the solar limb through the northern leg (A) after 01:29:48 UT. The spectral emissions and line-center intensities of all the Hα, Ca II 8542 Å and He I 10830 Å lines decreased (Figures 2(r)–2(z) and 3(r)–3(z)). The Doppler widths of these lines also decreased even though the profiles are still rather wide (Figures 3(r)–3(z)).

Comparisons of the spectrograms taken at 01:25:38 and 01:27:08 UT with those at 01:29:48 and 01:33:06 UT demonstrated that mass motions in both the northern and southern part of flare have changed their directions. Namely, the mass motion in northern part changed from toward the observer to away from the observer, whereas the mass motion in the southern part just underwent the opposite change. These changes presumably imply the rotating structures and motions of the flaring plasma.

3.2. SPACE OBSERVATIONAL RESULTS

We do not have high spatial resolution observations from TRACE because it was pointed to another region during the flaring period. Fortunately, we have full-disk EUV images at 195 Å from EIT/SOHO, which show the flare and its loop structures clearly even though its spatial resolution is not very high (Figures 4(a) and 4(d)). The flare was also observed by RHESSI. We reconstructed RHESSI images in the energy bands of 3–12, 12–25 and 25–50 keV. The reconstructed RHESSI images in 3–12 keV and 12–25 keV energy bands show two separate thermal sources clearly. But no non-thermal source was found in the images of 25–50 keV energy band. Some results are shown in Figure 4. The energy spectrum analysis of RHESSI data gives a thermal spectrum. The derived maximum temperature and emission measure (EM) are 3.2×10^7 K and 0.0026×10^{49} cm^{-3}, respectively, which are different from the inferred values of 1.45×10^7 K and 0.78×10^{49} cm^{-3} from GOES-10 data.

The flare loop structures in Hα and EUV 195 Å are generally similar (Figure 4(a)), but the high temperature loops in the EUV are more complicated than the Hα loop. This indicates that the high-temperature flaring plasma was distributed more inhomogeneously than low-temperature plasma in Hα. The EUV emission at the southern footpoint (B1 + B2) is more intense than elsewhere, which spatially corresponds to the stronger 12–25 keV source (S2) from RHESSI (Figures 4(b) and 4(c)) (actually it represents high-temperature plasma emitting soft X-ray (SXR)). Figure 4(a) also shows a connection between the main flare loop and the southern part (B2) of the south footpoint of the loop, which was not seen in Hα images (Figures 1(d)–1(f)). The relatively weaker 12–25 keV source (S1) is located in this region (Figure 4(b) and (c)). Figures 4(b) and 4(c) also demonstrate similar motion of the outer 12–25 keV source (S1) to that reported by Gallagher *et al*. (2002) for the

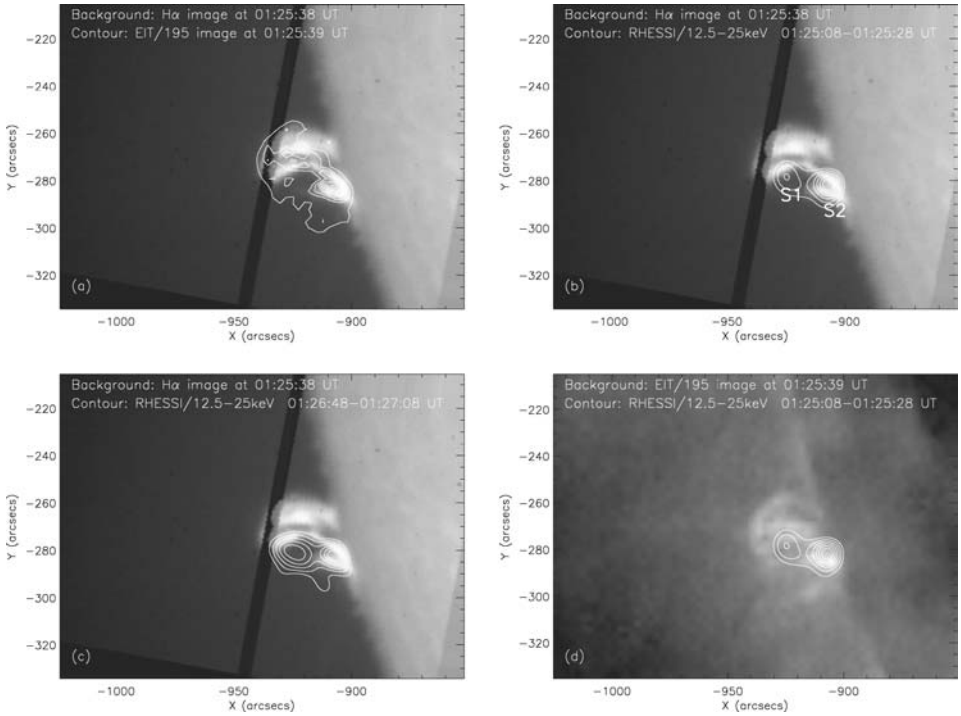

Figure 4. (a) The EIT 195 Å image at 01:25:39 UT (contour) superposed on the slit-jaw Hα image at 01:25:38 UT; the RHESSI 12–25 keV image at (b) 01:25:08–01:25:28 UT (contour) and (c) 01:26:48–01:27:08 UT superposed on the slit-jaw Hα image at 01:25:38 UT; (d) the RHESSI 12–25 keV image at (b) 01:25:08–01:25:28 UT (contour) superposed on the EIT 195 Å image at 01:25:39 UT. The contour levels of RHESSI images are 40, 50, 60, 70, 80 and 90% of the maximum image value.

X1.5 flare of 21 April 2002 and the increase of its intensity with respect to the inner source (S2).

3.3. Distributions of velocity and Doppler width

Using the observed spectral data of the three lines, we studied the distributions of the line-of-sight velocities and relative Doppler widths defined as $\Delta\lambda_D/\lambda$ along the slit at four different times that were indicated in Figure 1. In order to derive the line-of-sight velocities and the Doppler widths of the observed profiles, for the first step, we use Doppler broadening and a uniform flare model to simulate the observed profiles, i.e., we fit Gaussian profiles to observed ones. In practice, for a limb flare with Doppler broadening and a uniform flare model, the line intensity can be expressed as

$$I_\lambda = S_\lambda(1 - e^{-\tau_\lambda}), \tag{1}$$

where S_λ is the source function. The optical thickness for Hα and Ca II 8542 Å lines, given the line-center optical thickness τ_0, can be written as

$$\tau_\lambda = \tau_0 e^{-\frac{(\Delta\lambda-\Delta\lambda_0)^2}{\Delta\lambda_D^2}}, \qquad \Delta\lambda_D = \sqrt{\frac{2RT}{\mu} + \upsilon_t^2} \tag{2}$$

and for He I 10830 Å triplet

$$\tau_\lambda = \tau_{01}\left[e^{-\frac{(\Delta\lambda-\Delta\lambda_0)^2}{\Delta\lambda_D^2}} + 0.6\, e^{-\frac{(\Delta\lambda-0.091-\Delta\lambda_0)^2}{\Delta\lambda_D^2}} + 0.2\, e^{-\frac{(\Delta\lambda-1.26-\Delta\lambda_0)^2}{\Delta\lambda_D^2}}\right], \tag{3}$$

where $\Delta\lambda = \lambda - \lambda_0$, $\Delta\lambda_0 = \frac{\upsilon}{c}\lambda_0$ and λ_0 is the rest line-center wavelength, and υ and υ_t are the line-of-sight and turbulent velocity, respectively. τ_{01} in Equation (3) is the line-center optical thickness of the I_1 component (10830.341 Å) of the He I 10830 Å triplet.

In our calculations, we take the temperature to be 10^4 K and specify a set of S_λ, τ_0 (τ_{01} for the He I 10830 Å triplet), υ_t and υ. By trial and error method, we can get a set of parameters that best fit the observed profiles. The Doppler widths were computed by the formula in Equation (2). The uncertainties of the line-of-sight velocities estimated from the fitting is 4–6 km s^{-1}, which are mainly due to the wide profiles and the asymmetry of the observed profiles. We will give more discussion about measured line-of-sight velocities at the end of this section. The derived Doppler widths are related to the source functions (and temperature) and micro-turbulence velocities. However, for the wide profiles presented in this paper, the Doppler widths are not sensitive to the source function (and temperature). The estimated accuracies of the Doppler width measurements are within 4–7%.

The derived line-of-sight velocities (middle column) and relative Doppler widths (right column) along the slit at four different times together with the integrated line intensities (left column) are plotted in Figure 5. From the figure, we see that the distributions of the integrated line intensities, line-of-sight velocities and relative Doppler widths along the slit have the same tendency with some difference.

In the early phase of the flare (01:21:56 UT), the velocities along the slit (from the north to the south) show a roughly monotonic decrease (Figure 5(b)), whereas the integrated line intensity of He I 10830 Å increases and those of Hα and Ca II 8542 Å increase in the north part and decrease in the south part (Figure 5(a)). The corresponding Doppler width did not manifest large variation along the slit (Figure 5(c)) even though the Doppler width distribution of Hα has a peak at the distance of 13–16″ to the start points (marked '1' in Figures 1(b), 1(e), 1(h) and 1(i)). Figure 5(e) reveals the opposite rotating motion of the flare plasmas in the northern and southern legs of the flare loop at 01:26:28 UT (near the flare maximum). The Doppler widths of all the three lines at this time are doubled with respect to those at 01:21:56 UT, and Doppler widths of Ca II 8542 Å at some points are even tripled (Figures 5(c) and 5(f)). The widest profiles spatially correspond to the middle brightest part of Hα image (Figure 1(e)). Figures 5(e) and 5(f) also lead

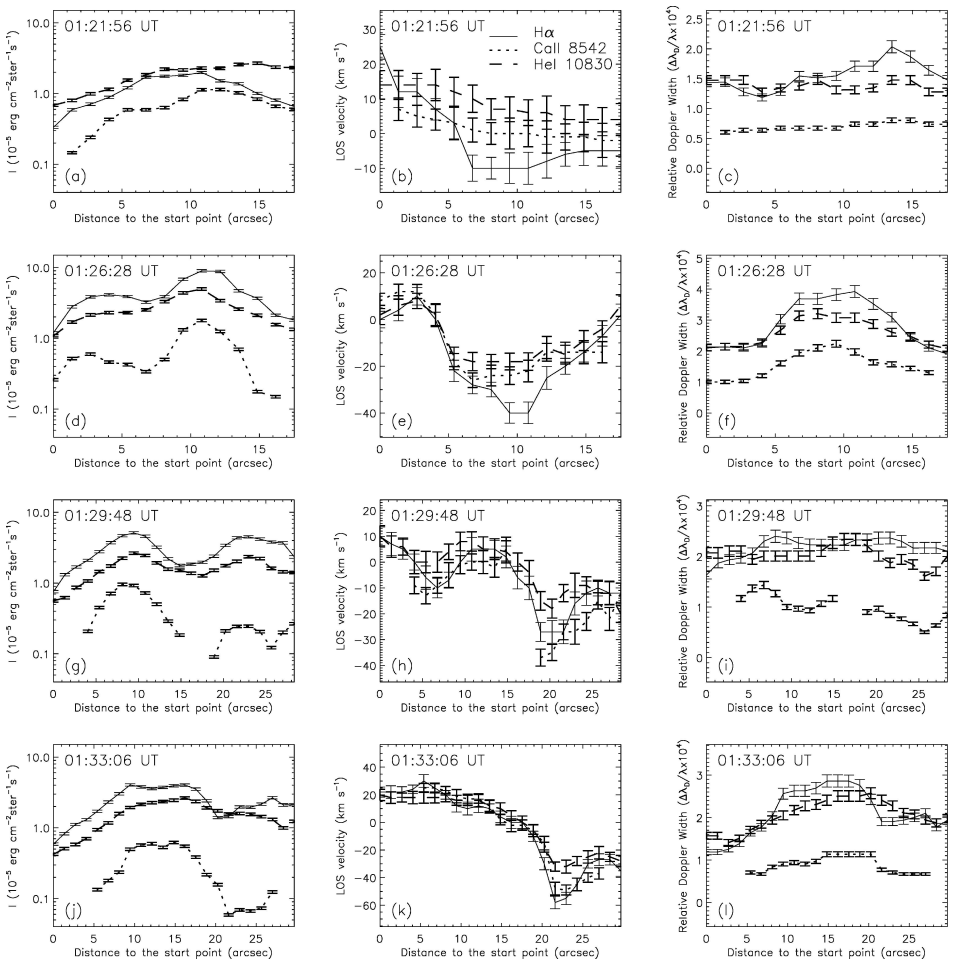

Figure 5. Distributions of the integrated line intensities (*left*), line-of-sight velocities (*middle*) and relative Doppler widths ($\Delta\lambda_D/\lambda$) (*right*) along the slit derived from the Hα (*solid line*), Ca II 8542 Å (*dotted line*) and He I 10830 Å (*dashed line*) spectral data at 01:21:56 UT (*first row*), 01:26:28 UT (*second row*), 01:29:48 UT (*third row*) and 01:33:06 UT (*last row*). Positive velocity that results in blue-shift of line-center is towards the observer. The start and end positions for these times are indicated by arrows and numbers in the Hα images in Figures 1(b), 1(e), 1(h) and 1(i), respectively. The missing data of Ca II 8542 Å in (g)–(i) imply that there is no Ca II 8542 Å emission.

to the result that the Doppler widths are possibly associated with the line-of-sight velocities.

Figure 5(h) also indicates the rotation of the plasma in the northern leg, but the rotating direction was reversed. Both the Doppler widths and their variations decreased at 01:29:48 UT (Figure 5(i)). The line-of-sight velocities from all the three lines at 01:33:06 UT have small difference, although there are large line-of-sight velocities (Figure 5(k)). The Doppler widths (Figure 5(l)) generally decreased

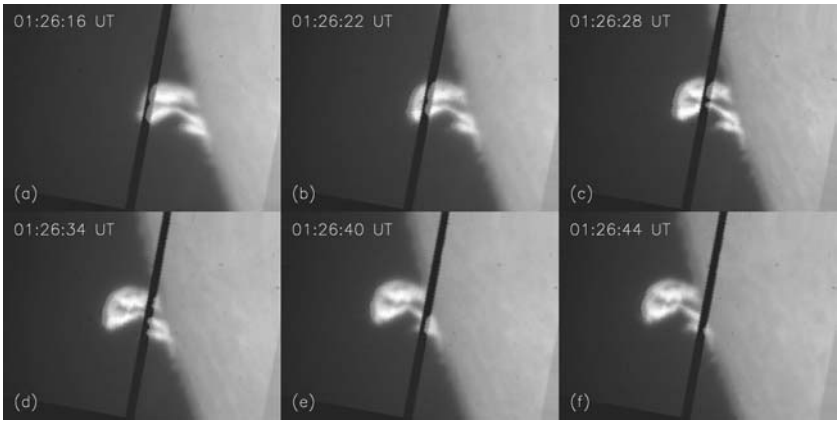

Figure 6. Same as Figure 1, but taken around the flare maximum.

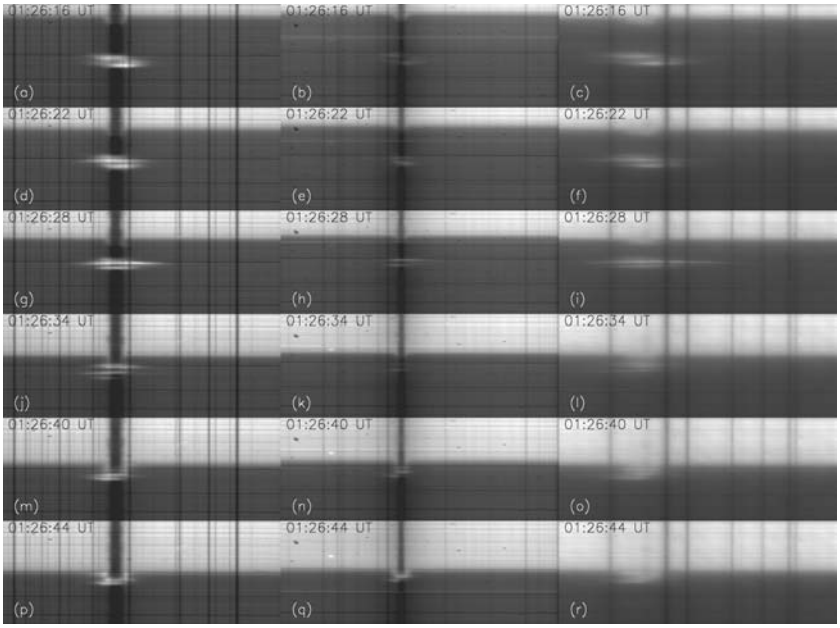

Figure 7. Same as Figure 2, but corresponding to Hα images in Figure 6.

except for some points that spatially correspond to the bright middle part of the flare in the Hα image (Figure 1(i)).

In order to further study the distributions of the line-of-sight velocities and Doppler widths in the flare, we selected six data sets observed in the period of 01:26:16–01:26:44 UT around the flare maximum. The slit cuts a different part of the flare loop in each Hα image. Shown in Figures 6 and 7 are the selected Hα images and corresponding spectrograms in the three lines. Figure 7 demonstrates that the

widest profiles were observed in the bright middle part of the flare where the line-of-sight velocities are large (Figures 6(c) and 7(g)–7(i)) and the rotating motions are small. In both the higher and lower parts of the flare, the rotating motions that lead to the tilted structures in the corresponding spectrograms are significant but have opposite rotating directions. The line profiles in the higher part (Figures 7(a)–7(f)) are wider than in the lower part (Figures 7(j)–7(o)). It is worth mentioning that the profiles at the southern footpoint of the flare loop that spatially corresponds to the RHESSI HXR source S2 are just moderately broadened (Figures 7(m)–7(r)).

To examine the reality and validity of the measured line-of-sight velocities, we made the following tests and measurements. There are two telluric lines (λ10832 and λ10834) in the red wing of He I 10830 Å line that can be used to check whether the measured evident line-of-sight velocities are due to instrument effects. We made 60 measurements of these two telluric lines using the disk-center spectrogram observed on the same day as the flare, and we did not detect any obvious line-of-sight velocity. It excludes the possibility that instrument effects lead to the large line-of-sight velocities. This is also confirmed by the plots in Figure 3 (right column), where the two telluric lines are always at the correct positions. We also applied our method to the spectral profiles of all the three lines observed in the disk-center quiet region on 1 August 2003 and the active region 10484 on 20 October 2003 to determine the line-of-sight velocities in quiet Sun and active regions with no flare. We made 100 and 90 measurements for the quiet and active regions, respectively. The measurements gave an average velocity of 1.8 ± 0.4 km s^{-1} and 2.9 ± 0.6 km s^{-1} for quiet and active regions, respectively. These values are much smaller than those derived from the flare spectral data. Based on the earlier discussion, we conclude that the measured line-of-sight velocities for the flare are real and believable.

4. Discussions and Conclusions

We reported the results from multi-wavelength observations of the C5.6 limb flare of 1 August 2003 including Hα, Ca II 8542 Å, He I 10830 Å, EUV and soft and hard X-rays. This flare manifested a rapid rising and expanding process in the impulsive phase and showed rather wide Hα, Ca II 8542 Å and He I 10830 Å profiles. The widest profiles were observed near the flare maximum in the middle part of the flare. Among the three lines, Ca II 8542 Å line shows the narrowest profile. For this flare, however, the FWHM ratio of the widest Ca II 8542 Å profile observed near the flare maximum to that of the widest Hα profile is 0.74, which is much larger than the value (0.29) of Ding *et al*. (1999) observed in the SF/C3.2 limb flare of 11 November 1998. Our previous work, Li and You (2001) demonstrated that for the He I 10830 Å line the Stark broadening effect will be significant only when electron density is greater than 10^{16} cm^{-3}, which is 3–4 orders higher than the generally recognized value of 10^{12}–10^{13} cm^{-3} in a flare. In other words, we cannot use Stark broadening to simultaneously simulate the observed Hα, Ca II 8542 Å

and He I 10830 Å profiles. We will study the possible broadening mechanisms for these profiles in detail elsewhere.

The calculated maximum Doppler widths for Hα, Ca II 8542 Å and HeI 10830 Å are 2.57, 1.91 and 3.47 Å. These Doppler widths require non-thermal motion (turbulence) velocities of 116, 67 and 96 km s^{-1}, respectively, provided the Doppler broadening of a uniform flare model is applicable and assuming a temperature of 10^4 K. These values are much larger than the commonly accepted ones, which presumably imply that there are violent turbulence and/or velocity gradients in this flare. The different broadening behavior of these lines probably indicates that they are formed in different fine structures that cannot be spatially resolved by current observations (Ding *et al*., 1999).

The distributions of line-of-sight velocities and relative Doppler widths ($\Delta\lambda_D/\lambda$) presented in Section 3.3 demonstrate significant rotation of the flaring plasma in the loop. The plasma in the northern and southern legs of the loop may have opposite rotating directions. The decreasing rotating angular speed with time possibly indicates the de-twisting of the magnetic field in the flare loop. The widest profiles were observed in the middle part of the flare instead of the flare loop top as mentioned by Ding *et al*. (1999). This is coincident with the large line-of-sight velocity.

The analysis of the temporal variations of the line-center intensities and the relative Doppler widths indicates that the line-center intensity of Hα increased significantly (up to 60%) in the impulsive phase, implying a possible quick increase of Hα source function, whereas those of Ca II 8542 Å and He I 10830 Å remained almost unchanged (Figures 3(c)–3(h)). However, the Doppler widths of all the three lines were doubled and that of Ca II 8542 Å even tripled. This reflects the quick heating of the chromosphere, and rapid rising and expanding of the flare loop.

The energy spectrum study of the RHESSI observation provides a thermal spectrum for this flare, which gives a temperature of as high as 3.2×10^7 K. The reconstructed RHESSI images in 3–12 keV and 12–25 keV clearly show two separate thermal sources S1 and S2 as indicated in Figure 4(b). The stronger source S2 is spatially consistent with the southern Hα loop footpoint (B1 + B2) and intense EUV emission. We have seen from earlier sections that the spectral emission in this region is not as intense as in the middle part and the profiles of all the three chromospheric lines are just moderately broadened with respect to the profiles observed in the middle bright area. This means that the line broadenings have nothing to do with the thermal source. This point was also illustrated by the dark cavity in the Hα images observed in the late impulsive and decaying phase of the flare. Even though the Hα dark cavity (Figure 1(d)) is spatially corresponding to the thermal source S1 with high temperature, but no spectral emission was observed in all the Hα, Ca II 8542 Å and He I 10830 Å lines because all these lines are formed in the chromosphere with temperatures less than 2×10^4 K. It is just the high temperature that makes the dark cavity appear in Hα images observed in the late impulsive and decaying phase of the flare.

No non-thermal HXR source was found in the RHESSI images, which possibly indicates that the released energy was transferred to the chromosphere by conduction. The stronger thermal source (S2) was located near and the weaker (S1) about 1.5×10^4 km above the solar limb (Figures 4(b) and 4(c)). Meanwhile, the location of S2 did not change in the flare process. We may speculate that the magnetic reconnection of this flare could take place in the lower solar atmosphere (Chen *et al*., 1999; Ji, Song, and Li, 2001).

Acknowledgements

We would like to thank the anonymous referee for his/her careful reading of this paper and valuable suggestions to improve the manuscript. SOHO is a project of international cooperation between ESA and NASA. This work was supported by the National Natural Science Foundation of China (NSFC, grant numbers 10273023 and 10333040), National Basic Research Priorities Project (G2000078402) of China.

References

Bentley, R. D., Doschek G. A., and Mariska, J. T.: 1996, *Adv. Space Res.* **17**, 55.
Brosius, J. W.: 2001, *Astrophys. J.* **555**, 435.
Canfield, R. C. and Gayley, K. G.: 1987, *Astrophys. J.* **322**, 999.
Chen, P. F., Fang, C., Ding, M. D., and Tang, Y. H.: 1999, *Astrophys. J.* **520**, 853.
Delaboudinière, J.-P., Artzner, G. E., Brunaud, J., Gabriel, A. H., Hochedez, J. F. *et al.* : 1995, *Solar Phys.* **162**, 291.
Ding, M. D., Liu, Y., and Chen, P. F.: 2002, *Solar Phys.* **207**, 125.
Ding, M. D., Fang C., Yin, S. Y., and Chen, P. F.: 1999, *Astron. Astrophys.* **348**, L29
Domingo, V., Fleck, B., and Poland, A. I.: 1995, *Solar Phys.* **162**, 1.
Falchi, A., Mauas P. H. J., Andretta, V., Teriaca L, Gauzzi G. *et al.* : 2003, *Mem. S. A. It.* **74**, 639.
Fang, C., Hénoux J.-C., and Ding, M. D.: 2000, *Astron. Astrophys.* **360**, 702.
Fang, C., Hénoux J.-C., and Gan, W. Q.: 1993, *Astron. Astrophys.* **274**, 917.
Gallagher P. T., Dennis B. R., Krucker S., Schwartz, R. A., and Tolbert A. K.: 2002, *Solar Phys.* **210**, 341.
Gu, X. M., Dun, J. P., and Zhong, S. H.: 2003, *New Astron.* **8**, 427.
Heinzel P.: 2003, *Adv. Space Res.* **32**, 2393.
Hénoux J.-C., Fang, C., and Gan, W. Q.: 1993, *Astron. Astrophys.* **274**, 923.
Ji, H. S., Song, M. T., and Li, X. Q.: 2001, *Solar Phys.* **198**, 133.
Kundu, M. R., Garaimov, V. I., White, S. M., and Krucker, S.: 2004, *Astrophys. J.* **600**, 1052.
Li, H. and You, J. Q.: 2001, *Astron. Astrophys.* **374**, 1121.
Li, H., Fan, Z., and You, J.: 1999, *Solar Phys.* **185**, 67.
Li, H., You, J., Yu, X. F., and Wu, Q. D.: 2002a, *Astron. Astrophys.* **391**, 741.
Li, H., You, J., Wu, Q. D., and Yu, X. F.: 2002b, *Chin. Phys. Lett.* **19**, 742.
Lin, R. P., Dennis, B. R., Hurford, G. J., Smith, D. M., Zehnder, A. *et al.* : 2002, *Solar Phys.* **210**, 3.
Liu, Y. and Ding, M. D.: 2002, *Chin. J. Astron. Astrophys.* **2**, 277.
Mariska, J. T.: 1994, *Astrophys. J.* **434**, 756.
Mein, P., Mein, N., Malherbe, J.-M., Heinzel, P., Kneer, F. *et al.* : 1997, *Solar Phys.* **172**, 161.

Morimoto, T. and Kurokawa, H.: 2003, *Publ. Astron. Soc. Jpn.* **55**, 505.
Qiu, J. and Gary, D. E.: 2003, *Astrophys. J.* **599**, 615.
Scherrer, P. H., Bogart, R. S., Bush, R. I., Hoeksema, J. T., Kosovichev, A. G. *et al.* : 1995, *Solar Phys.* **162**, 129.
Suemoto, Z. and Hiei, E.: 1959, *Publ. Astron. Soc. Jpn.* **11**, 185.
Švestka, Z.: 1976, *Solar Flares*, D. Reidel Publishers and Co., Dordrecht, The Netherlands.
You, J. Q., Wang, C. J., Fan, Z. Y., and Li, H.: 1998, *Solar Phys.* **182**, 431.
You, J. Q., Li, H., Fan, Z. Y., and Sakurai, T.: 2001, *Solar Phys.* **203**, 107.